

# Fast Pulse Generation for Single-Photon Atom Interferometry

Shaan Dias

*Carleton College Physics Department, Northfield, MN 55057*

Emmett Hough, Tahiyat Rahman, Richard Kim, Subhadeep Gupta

*University of Washington Physics Department, Seattle, WA 98195*

(Dated: September 3, 2024)

Within the toolbox for atom optics and interferometry, single-photon processes enable faster transitions between atomic states than two-photon processes, allowing for faster momentum transfer and shorter overall atom interferometer sequences. Here we develop a system to generate fast pulses of 556 nm (green) light on the  $^1S_0 - ^3P_1$  ytterbium transition, with high enough power to drive complete transfers in 15 ns. These pulses will be used for single-photon atom interferometry with ytterbium atoms with large momentum separation in a fast, compact configuration, suitable for sensitive gravimetry and accelerometry.

## I. INTRODUCTION

Atom interferometry is a powerful tool for making precision measurements for fundamental physics and inertial sensing. Utilizing the fact that matter exhibits wave-like properties, an atom interferometer (AI) sends atoms along various paths through space-time before recombining them to produce an interference pattern. These interference fringes enable us to make sensitive measurements of atomic properties and external forces to the benefit of a variety of fields including navigation, geophysics, metrology, and tests of fundamental physics [1]. For instance, current state-of-the-art inertial sensing can measure accelerations at the  $2 \times 10^{-8}$  m/s<sup>2</sup> level while reaching stability of  $5 \times 10^{-10}$  m/s<sup>2</sup> in  $10^5$  s [2, 3].

To do this, we utilize a two-level quantum system and use photons to coherently drive atoms between the two states, while also imparting momentum to them. By using the concept of Rabi oscillations, we can carefully tune the duration of the laser pulse to control the probability of making such a transition. We call a  $\pi$  pulse one which results in a complete transfer of population from one state to another, and a  $\pi/2$  pulse one which results in superposition of the two populations with equal amplitudes [4]. As depicted in Figure 1 in the prototypical AI configuration known as a Mach-Zehnder, a  $\pi/2$  pulse puts the atom in an even superposition of the two states (analogous to a beam splitter), and a  $\pi$  pulse flips the states (analogous to a mirror). Then the interferometer is closed with another  $\pi/2$  pulse and the resulting interference pattern, created by the difference in phase accumulated along each of the two paths, can be read off.

The sensitivity of these measurements is proportional to the space-time area enclosed by the arms of the interferometer. As such, physicists are interested in finding ways to increase the space-time area that the interferometer encloses. One class of methods is termed large momentum transfer (LMT) atom interferometry, in which additional light pulses are used to impart higher momenta on the interferometer arms, thus increasing the

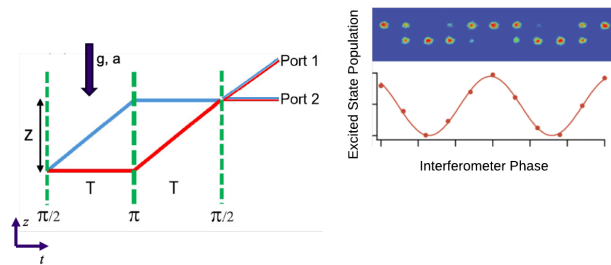


FIG. 1: Mach-Zehnder interferometer geometry, driven by a sequence of pulses  $\pi/2 - \pi - \pi/2$  for a total interrogation time  $2T$ . The interference pattern is read off of either port, and its phase can be used to make sensitive measurements of atomic properties and external forces.

distance they travel. To understand why this helps, consider measuring the acceleration due to gravity  $g$ . To make a good measurement, we want to have a small uncertainty compared with the value of  $g$ . For our measurement, this means we need a small uncertainty in the phase  $\phi$  compared with the value of  $\phi$ . For a standard vertically oriented Mach-Zehnder interferometer, the phase difference between the two paths goes as  $nk_gT^2$ , where  $n$  is the number of recoil momenta and  $T$  is the time between  $\pi/2$  and  $\pi$  pulses. The shot noise uncertainty in phase goes as  $\frac{1}{\sqrt{N}}$  where  $N$  is the number of atoms. Thus, increasing space-time area improves the measurement since

$$\frac{\delta g}{g} = \frac{\delta \phi}{\phi} = \frac{1}{\sqrt{N}nk_gT^2}. \quad (1)$$

Our group has passed several milestones in previous work using ultracold ytterbium (Yb) atoms, which is an alkaline-earth-like metal. Our group demonstrated the second ever Yb BEC in 2011 [6], and the first Yb interferometer in 2014 [7]. Following that work, we explored a new method to measure the fine-structure constant by using Bragg transitions to create a then-record 112 recoil

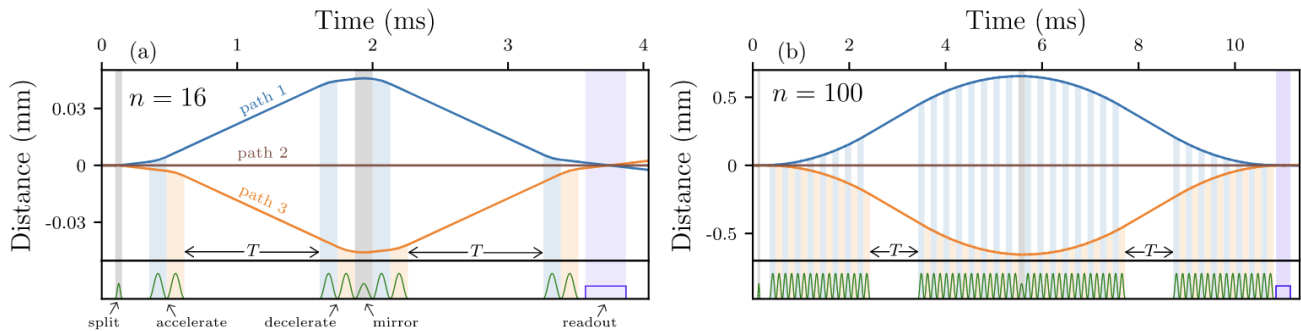


FIG. 2: Figure from [5] depicting three-path atom interferometry space-time trajectory and atomic optics sequence for (a)  $n = 16$  and (b)  $n = 100$  using two-photon processes. This method has successfully achieved LMT up to  $n = 112$ .

LMT AI [5]. We also reported the first fountain AIs for Yb [8]. Yb is advantageous for its multiple available isotopes (which allows for equivalence principle testing and systematic cross-checks) and its narrow-linewidth transitions that could be used for single-photon AI, making it a good choice for this application.

In this report, I will first discuss the underlying physics of atom interferometry as a whole, with a focus on how we will implement single-photon LMT atom interferometry. I will then report on the initial work I have accomplished to generate the fast laser pulses required to achieve the results we are interested in, and then discuss the future work still required.

## II. SINGLE-PHOTON LMT CLOCK AI

### A. 2-Photon vs Single-Photon Processes

Currently the most common way of doing AI is to use a 2-photon process. An example of which called a Bragg transition is shown in Figure 3a where the ground state and excited state are plotted in momentum space, so they lie on the dispersion relation given by the kinetic energy  $p^2/2m$  plus the internal energy, where  $p$  is the momentum of the atom cloud and  $m$  is the mass of Yb. In the 2-photon process, using two lasers, the atom is driven from the ground state up to some energy far detuned from the excited state, and then back down to the ground state. In this process, the atom gains two recoil momenta ( $2\hbar k$ ) from the photons.

Additionally, LMT is possible with 2-photon processes, in which to gain  $2n\hbar k$  recoil momenta, you repeat this transition  $n$ -many times as shown in Figure 3b. In our lab, using this method we have demonstrated up to 112  $n$ , using the interferometer geometry shown in Figure 2 [5]. By now, the Bragg transition process is well understood for large momentum transfer, but it has certain limitations.

For instance, there is a limit on how fast the  $\pi$  pulses can be. If you consider the Fourier transform limit, if you

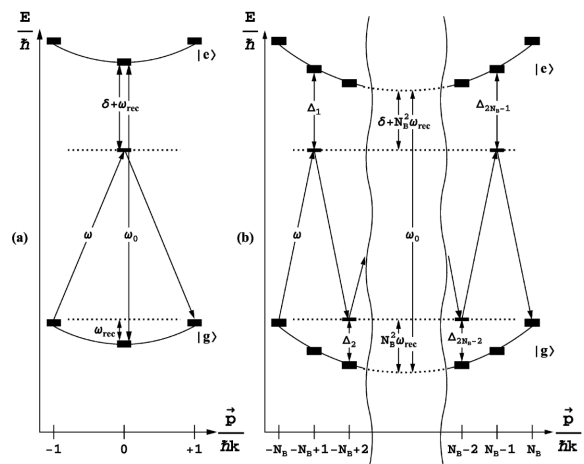


FIG. 3: Figure from [9] depicting 2-photon (a) first- and (b)  $N_b$ -th-order Bragg transition diagram. The atomic kinetic energy states of momenta  $N\hbar k$  lie along the parabola  $N^2\hbar\omega_{\text{rec}}$ , where  $\omega_{\text{recoil}} = \frac{\hbar k^2}{2m}$  and  $N = 0, \pm 1, \pm 2, \dots$ . Atoms are driven between these states by two photons, gaining  $2\hbar k$  recoil momenta in the first-order transition and  $2N_b\hbar k$  recoil momenta in the  $N_b$ -th-order transition.

have a very fast pulse in time, then you must have a large spread in frequency. In the 2-photon process, all the relevant ground states have very closely spaced energies, on the order of  $\omega_{\text{recoil}} = \frac{\hbar k^2}{2m}$ . So if the frequency bandwidth is greater than this energy spacing, the pulse will address multiple possible transitions and send some of the atoms to different states, causing you to lose coherent control in the system. Using photons of wavelength  $556\text{nm}$  with Yb, we find  $\omega_{\text{recoil}} = 2\pi \times 3.71$  kHz sets the upper bound for our frequency spread.

Additional LMT techniques exist such as Bloch Oscillations, in which atoms are manipulated via two counter-propagating lasers with a time-varying detuning. This induces the atoms to Bloch oscillate about the periodic



put some numbers to it, to achieve momentum separation of  $100 \hbar k$  requires  $50 \pi$  pulses, so each  $\pi$  pulse would need to be on the order of 10 ns. Tuning a  $\pi$  pulse depends on both the duration and the intensity of the light, so our goal in this project is to find a way to generate pulses of 556 nm light that are on the order of 10 ns with high enough power.

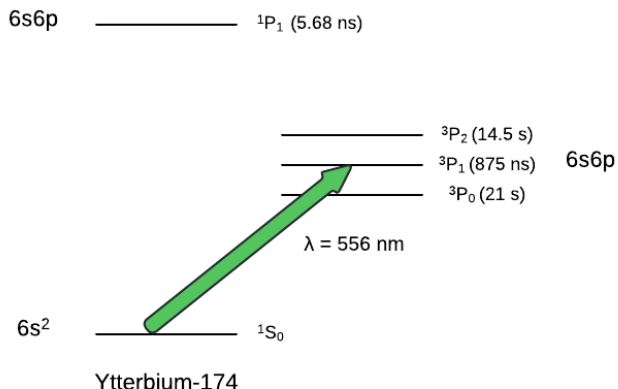


FIG. 6: Energy level diagram of the relevant  $^{174}\text{Yb}$  states. We aim to perform LMT interferometry on the  $^1S_0 - ^3P_1$  transition to take advantage of its narrow linewidth.

Also worth noting, the reason we do not use one of the longer lifetime states in Figure 6 such as the  $^3P_0$  (which would allow more time to do LMT), is that the longer lifetime transitions are much more strongly forbidden. Thus, they have much lower Rabi frequencies, so driving the longer lifetime transitions requires much longer  $\pi$  pulses or more intense light. As a result, there is a trade-off to be had, which is why the shorter lifetime state can actually be preferred, especially for compact experiments such as our own in which we want to be very fast.

#### D. Implementing an Acousto-Optic Modulator

The key device to generate these pulses is an acousto-optic modulator (AOM), shown in Figure 7. To operate it, you send an oscillating voltage signal to a transducer, which converts the signal into a sound wave that travels through a crystal. You then feed the light beam into the crystal and it Bragg diffracts off the sound wave, and resulting in various orders of diffracted beams coming out. Another key function of an AOM is that each diffracted beam's frequency is shifted based on the acoustic frequency. This can be understood from principles of conservation of energy and momentum by adding the phonon and photon wave vectors such that the first order beam gains the momentum of a single phonon, the second or-

der beam gains the momentum of two phonons, and so on.

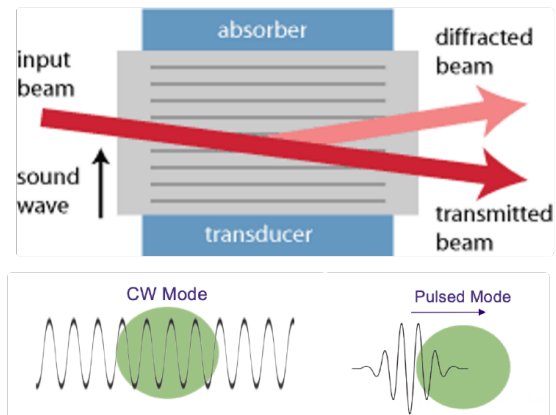


FIG. 7: Schematic diagram from [14] showing the function of an AOM. A transducer converts an oscillating voltage signal into a sound wave off of which the input laser beam diffracts. Achieving high power efficiency requires many nodes for the light to diffract off of, as shown in both continuous wave mode and pulsed mode.

In order to achieve good power efficiency into the diffracted beam, we can consider what the cross-section in continuous wave mode looks like, as in Figure 7. One thing we might consider is to have our beam to cover as many nodes as possible, such as by increasing the size of the beam, since more nodes results in more efficient Bragg diffraction. However, we will operate the AOM in pulsed mode, sending pulses of sound in to get pulses of diffracted light out. In this picture, if the beam is bigger than the wave packet itself, then only a fraction of the light is interacting with the sound wave at any time, so a larger beam input will limit the power efficiency. So there's some balance to be found for the beam to be big enough to interact with many nodes, without being much bigger than the wave packet itself, in order to get optimal power efficiency.

Additionally, the rise time of the pulse goes as  $t_r \sim \frac{D}{V}$ , where  $D$  diameter of the input beam and  $V$  is the speed of sound in the crystal. Essentially the rise time is the time it takes for the sound wave to travel across the beam. You cannot control the speed of sound, but this gives another indication that we want to limit the size of the beam.

Furthermore, the phase of the laser pulses generated is an important variable, given that the phase of the pulses contributes to the phase of the eventual interference pattern. Thus, having the ability to know and control the phase of each pulse is crucial in order to vary the phase of the interferometer, measuring the resulting population distributions to produce a fringe. So an important con-

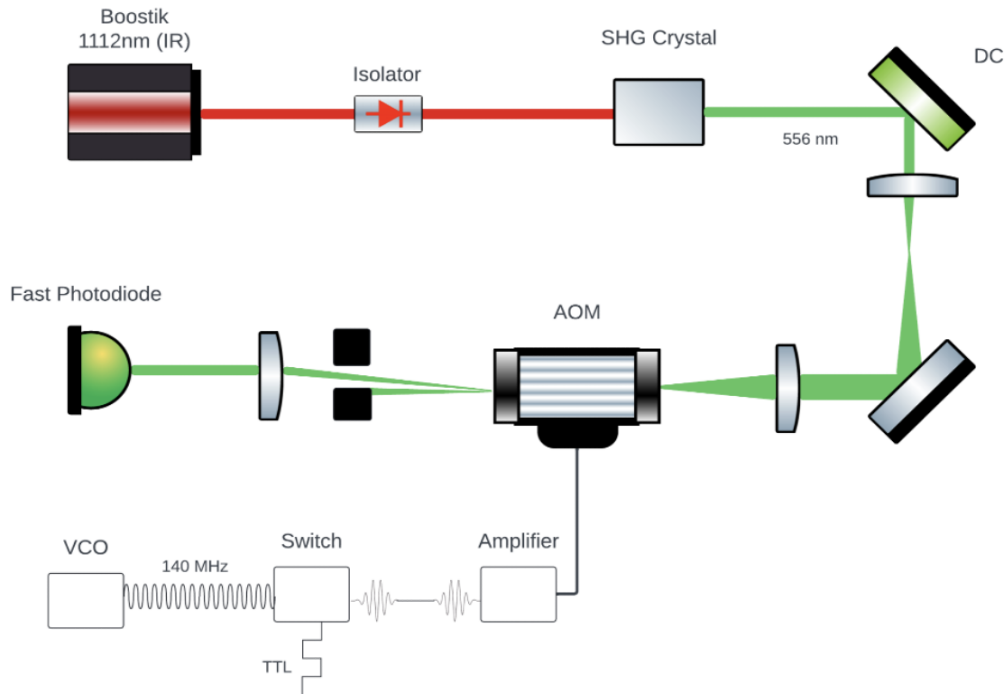


FIG. 8: Schematic diagram of experimental setup. 1112 nm infrared light is converted to 556 nm green light via a second harmonic generation crystal, then isolated via a dichroic mirror. Green light is then focused down into the AOM, and the first order diffracted beam is picked off. The RF signal originates from a voltage controlled oscillator, and a switch is quickly turned on and off using a TTL signal to produce short RF wave packets which are amplified and then sent to the AOM. These RF voltage packets are converted to sound wave packets off which the green light diffracts, producing fast pulses in the first order diffracted beam.

sideration regarding the implementation of these pulses is to have robust reproducibility and tunability in the phase of each pulse.

### III. GENERATING FAST PULSES

#### A. Experimental Setup

Here we will outline the basic experimental setup used to implement all of this as depicted in Figure 8, and the following sections will provide more detail on the iterative process that led to these specific choices. On the optics side, we start with an infrared laser (Koheras Boostik BoY10PztS), and use a second harmonic generation crystal to double the frequency and generate 556 nm green light. We then use lenses to manipulate the size of the beam and focus down to an AOM (Crystal Technology, Inc model 3200-147), where the beam waist is roughly 30 microns. Then we take the first order diffracted beam and send it to a fast photodiode (Thorlabs PDA10A2) in order to read off the signal.

On the electronics side, we start with a voltage-controlled oscillator (Mini-Circuits ZOS-200) which generates a continuous RF signal with a tunable frequency.

We send that signal through a switch (Mini-Circuits ZASW-2-50DR), which can be turned on and off quickly using an input TTL. For initial testing, we have built a circuit that generates 2V peak TTL signals with a rise time of less than 10 ns. This allows us to generate RF wave packets coming out of the switch with a rise time of 10 ns, which is this switch's limit and the current limit on our overall setup. We then feed those RF packets into an amplifier before sending them to the AOM, so that the diffracted light pulses also have a rise time of 10 ns.

#### B. Optimizing Second Harmonic Generation Crystal

The first step in setting up this system is to optimize the second harmonic generation (SHG) crystal in order to produce adequate green light to work with, on the order of a few mW. In the SHG crystal, two input photons of the same wavelength are combined in a nonlinear process to produce a photon with half the wavelength, or twice the frequency. The rate at which this process occurs is dependent on the temperature of the crystal, so this is one of the first parameters to tune.

However, we first need to align the input beam such that there is an output signal to optimize. Our SHG

works by feeding the input light through the crystal via an optical fiber, so once the IR light is adequately coupled into this fiber, the crystal produces and emits green 556 nm light. The light is coupled into the fiber via a cylindrical lens, which is highly sensitive to the angle and z-position. Thus, optimizing this coupling requires walking the lens along the z-direction in small increments, and aligning the input beam at each step. Once the output power is maximized, the input alignment should be left alone as it is highly sensitive and easily falls out of alignment when touched.

We are next able to optimize the temperature by reflecting the output light off a dichroic mirror, as shown in Figure 8, to isolate the green light from the IR such that we can measure just the green power. In Figure 9, we see that the SHG crystal performs optimally around 42°C, roughly following a sinc<sup>2</sup> form.

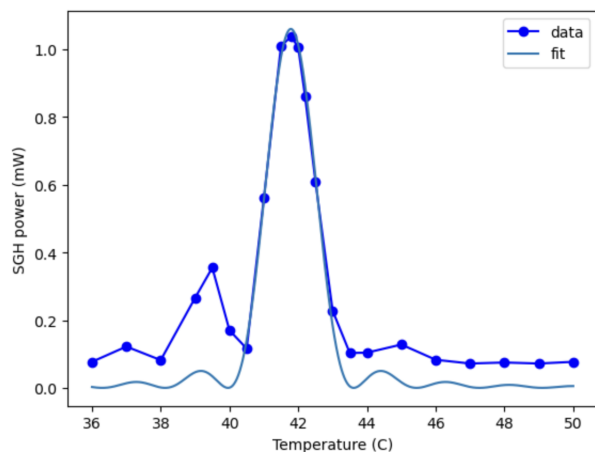


FIG. 9: Plot showing output green light power from SHG crystal as a function of crystal temperature, where we see that the crystal performs optimally just below 42°C.

Additionally, we expect that the power output should scale quadratically with the power input. At higher input powers, this relation will flatten out as the source of input photons is depleted and the system effectively saturates. This relation is confirmed in Figure 10.

### C. Characterizing Electronics

Now that we have a source of green light, the next step was to characterize the electronics we had, identify the limitations, and upgrade as needed. Using mirrors and lenses, we focused the green light down into the AOM. On the electronics side, we had a Mini-Circuits ZX80-DR230+ switch and a Thorlabs DET36A photodiode. Then, using a Moku:Go from Liquid Instruments, we could generate a TTL signal to turn on and off the switch, and also to read the signal off of the photodiode.

By observing the signal coming out of the switch, we

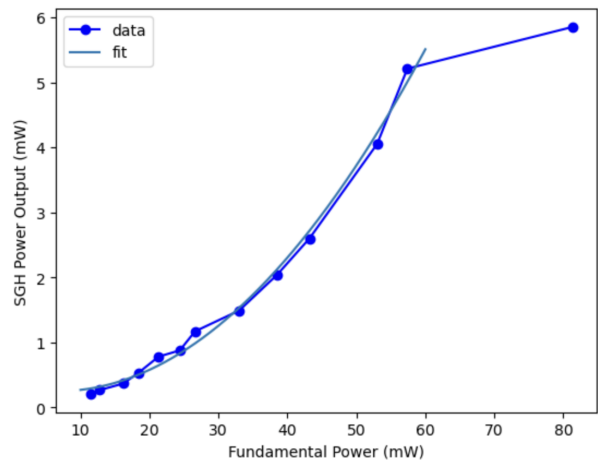


FIG. 10: Plot showing output green light power from SHG crystal as a function of IR power, where we confirm that the crystal output power scales quadratically with the input power, up to a point at which the system saturates as the source of input photons is depleted.

measured its rise time at around 1μs, matching the specifications given on its data sheet. We identified this as the main limiting factor, given that the photodiode rise time was around 40 ns. To upgrade, we replaced the switch with a Mini-Circuits ZASW-2-50DR switch. By looking at the RF packet it outputs, we measured this switch to have a rise time of 10 ns, agreeing with the provided specifications. This should be sufficient to achieve our 10 ns pulse goal.

However, the photodiode still required some improvement in order to accurately observe our pulses at these time scales. To address this, we purchased a Thorlabs PDA10A2 photodiode, which has a 2.3 ns rise time and a fixed gain amplification.

### D. Further Focusing Beam

In order to control the AOM rise time, we needed to control the waist size of the beam at the AOM, given that  $t_r \sim \frac{D}{v}$ . With Gaussian beams, focusing a beam with an initial diameter  $D$  and wavelength  $\lambda$  through a lens with a focal length  $f$  gives a waist

$$w_0 \approx \frac{2\lambda f}{\pi D}. \quad (2)$$

In my initial setup, I had  $D = 2.34$  mm and  $f = 150$  mm, which theoretically should focus down to a waist of 22.7μm. In order to confirm this, I took a pinhole beam profile. This method utilizes the fact that the radial irradiance of a Gaussian beam goes as

$$I(r, z) = I_0 \exp\left(\frac{-2r^2}{w(z)^2}\right) \quad (3)$$

where  $I_0$  is the peak irradiance at the center of the beam,  $r$  is the radius, and  $w(z)$  is the beam radius in the  $z$ -direction given by

$$w(z) = w_0 \sqrt{1 + \left(\frac{\lambda z}{\pi w_0^2}\right)^2}. \quad (4)$$

Feeding the beam through a pinhole of known size at various  $z$ -positions allows us to fit the power output to this known curve and back out the beam waist  $w_0$ . This is shown in Figure 11, passing the beam through a  $20\ \mu\text{m}$  pinhole, which allows us to determine the beam waist of  $25.90 \pm 0.58\ \mu\text{m}$ . This matches the theoretical prediction of  $22.7\ \mu\text{m}$ , and allows for a rise time at the AOM of around 6 ns.

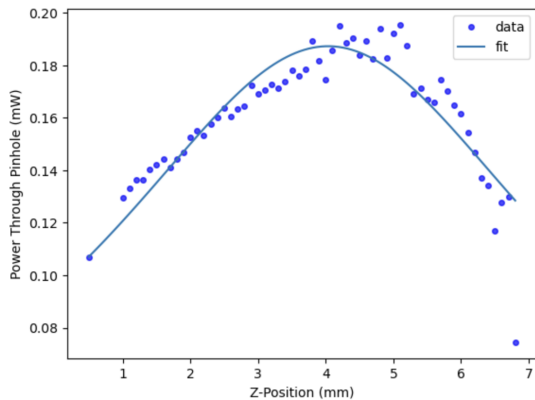


FIG. 11: Pinhole beam profiling of beam waist. By measuring beam power out of known  $20\ \mu\text{m}$  pinhole placed at various  $z$ -positions, we extrapolate the beam waist of  $25.90 \pm 0.58\ \mu\text{m}$ .

In order to explore the capabilities of the system and achieve an even faster rise time, we attempted to focus down even further. To achieve this, we allowed the input beam to double in size to  $D = 5\ \text{mm}$ , maintaining the lens with  $f = 150\ \text{mm}$ . This produced a  $11.23\ \mu\text{m}$  beam waist as shown in Figure 12, which would allow for a 2.5 ns rise time that would be more than sufficiently fast.

Note, however, that the  $25.90\ \mu\text{m}$  beam has a Rayleigh range of  $z_R = 3.8\ \text{mm}$  while the  $11.23\ \mu\text{m}$  beam has a Rayleigh range of just  $z_r = 0.7\ \text{mm}$ , where Rayleigh range

$$z_R = \frac{\pi w_0^2}{\lambda} \quad (5)$$

gives the distance from the focus in the  $z$ -direction at which the beam area doubles.

Having a larger Rayleigh range has certain benefits. Since the AOM has a finite width, the rise time really depends on the average beam size across the AOM. Thus, a beam with a small waist and short Rayleigh range could have a larger average beam size over the AOM than a beam with a larger waist but longer Rayleigh

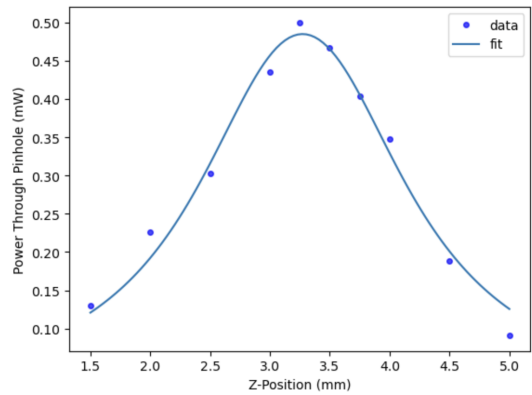


FIG. 12: Pinhole beam profiling of beam waist after focusing down further. Beam waist is now measured at  $11.23 \pm 0.46\ \mu\text{m}$ .

range. Moreover, by focusing down so aggressively to achieve such a small beam waist, Bragg selection can cause lowered diffraction efficiency because there is a spread in the transverse component of  $\mathbf{k}$ -vectors, meaning that the Bragg condition cannot be satisfied across the beam. We observed this effect in Figure 13, where the dark stripe across the beam is the component that meets the Bragg condition and diffracts. Also noticeable in Figure 13 is that the 0th and 1st order beams exiting the AOM overlap, again due to the short Rayleigh range, making it challenging to cleanly isolate the 1st order diffracted beam. For these reasons, we reverted back to the  $25.90\ \mu\text{m}$  beam, which will still be fast enough but with better power efficiencies and beams that are easier to spatially isolate.

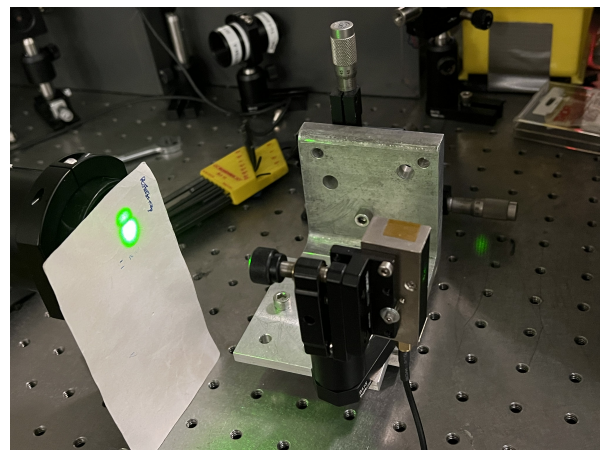


FIG. 13: Input beam undergoing Bragg selection at AOM. The  $11.23\ \mu\text{m}$  beam waist is small to the point that the transverse component of  $\mathbf{k}$ -vectors of light cannot all meet the Bragg condition. The result is that only the dark stripe across the beam meets the Bragg condition and diffracts, and the overall diffracted efficiency is worse.

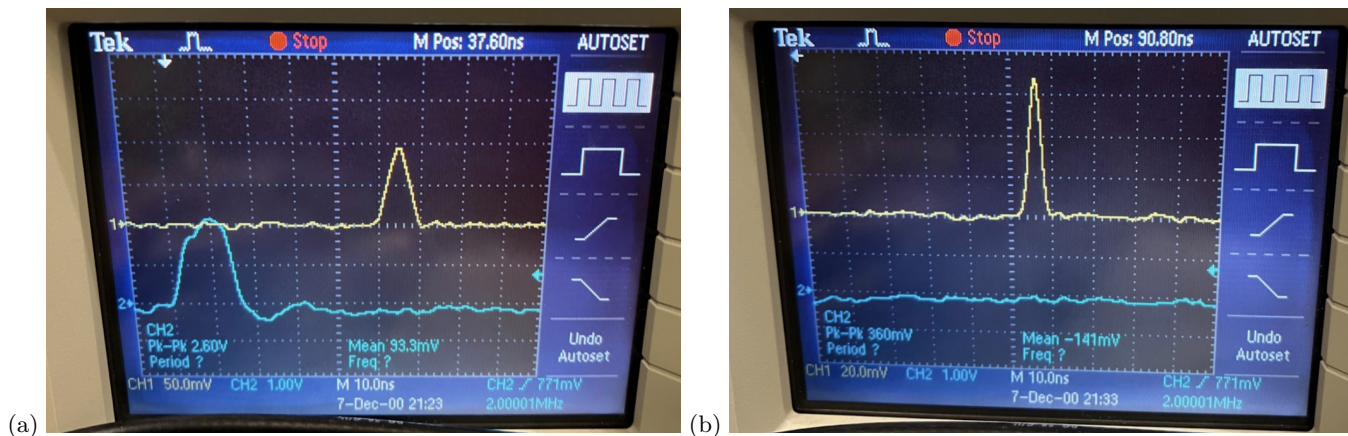


FIG. 14: Using an RF mixer, we view the RF wave packet amplitude (shown in yellow) (a) after the switch but before the amplifier and (b) after the amplifier, each triggered by a 10 ns rise time TTL input to switch (shown in blue).

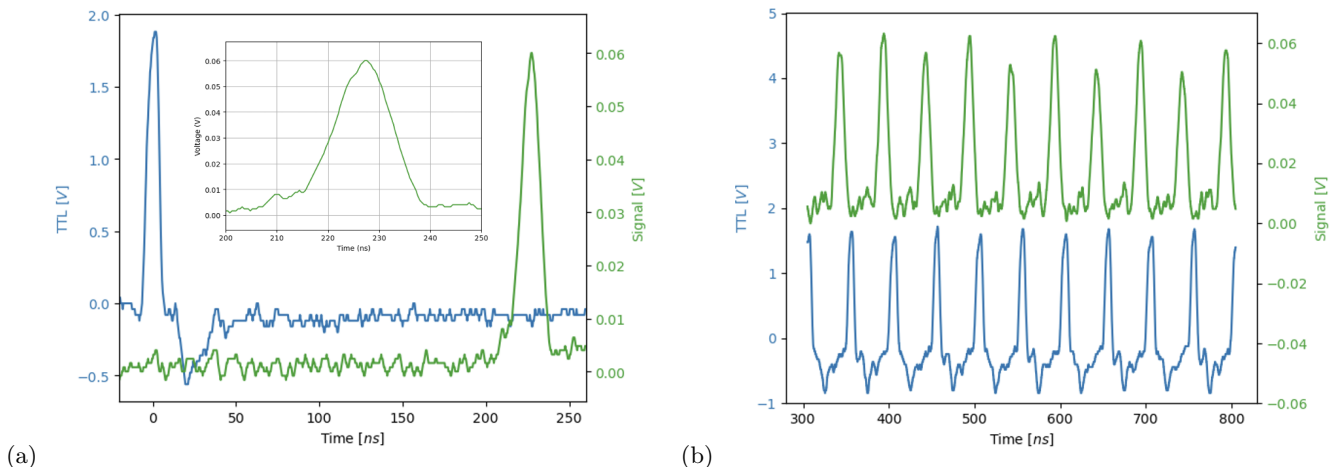


FIG. 15: Fast pulses in diffracted beam (green) following TTL signal at switch (blue). (a) Single fast pulse, inset zooms in on the diffracted pulse to confirm rise time of 10 ns. (b) Series of fast pulses generated by a corresponding series of TTL signals.

### E. Producing Fast Pulses

At this point, the slowest component in the system is the switch which has a rise time of 10 ns. Using a homemade circuit developed by group member Richard Kim, we can send the switch a TTL signal with a rise time less than 10 ns, which should result in RF packet outputs with a rise time of 10 ns, as limited by the switch. This is confirmed in Figure 14 in which, by using an RF mixer, we view the amplitude of the RF wave packet (rather than the individual oscillations). In Figure 14a, we see the RF packet after the switch in yellow, and the TTL input to the switch in blue. Figure 14b shows the RF packet after the amplifier in yellow. In both, we confirm that the rise time is 10 ns as expected. However, it is also worth noting that there is lots of variation in the shape and height of these RF packets. This is likely due to imperfections from the switch, and given that the switch

is also the limiting factor regarding pulse rise time, this will be an important component to further improve in the future.

We then send these amplified RF packets to the AOM and get pulses of diffracted light out, as shown in Figure 15 where the TTL input to the switch is shown in blue and the diffracted pulse out of the AOM is in green. In Figure 15a, the inset zooms in on the green peak to show the rise time of roughly 10 ns. Figure 15b shows that a series of TTL signals will result in a series of diffracted pulses as well.

Next, we coupled the diffracted beam into a test optical fiber (Thorlabs PM-S405-XP). In the eventual implementation, a similar fiber will be used to deliver the light to the atoms, so we are interested in seeing how the pulse profile changes after the fiber. The result is shown in Figure 16 with the pulse before the fiber in green and after the fiber in purple. In Figure 16a, we see an overall

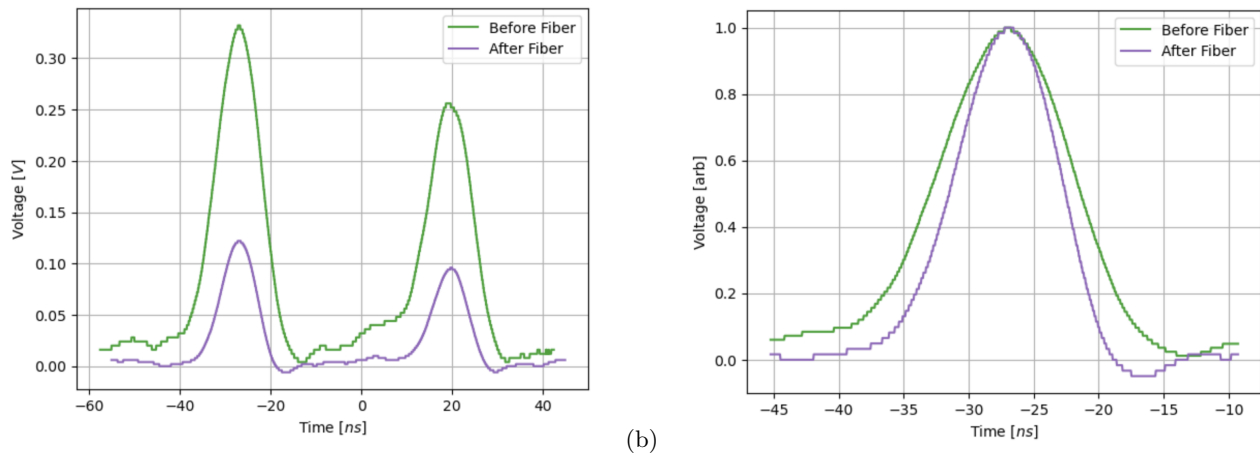


FIG. 16: Laser pulses before (green) and after (purple) coupling to an optical fiber. (a) The power output after the fiber is around 40%, as expected. (b) The normalized pulse profiles show a decrease in rise time after the fiber by around 20%, since fiber coupling depends on both the input power and beam mode.

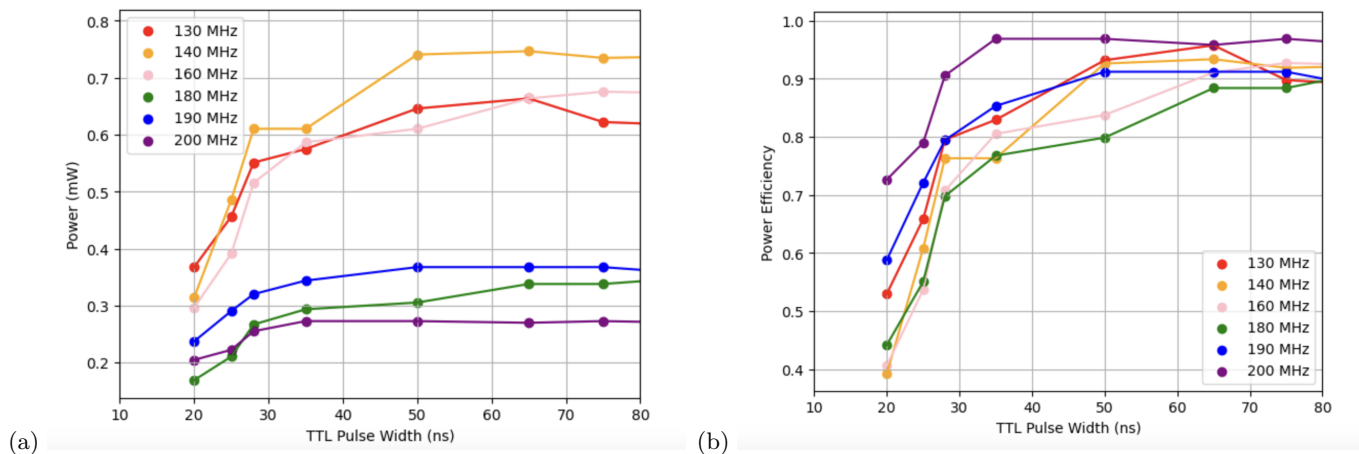


FIG. 17: Power output in diffracted beam as a function of TTL pulse width (and thus sound packet width) and RF frequency. (a) This AOM performs best at 140 MHz, suggesting that it has a center frequency of 140 MHz. For shorter pulses, power output decreases as there are less nodes for the light to diffract off. (b) The power efficiencies when normalized to the continuous wave output show higher efficiencies for higher frequencies, again explained by having more nodes at short pulses.

power loss of around 40%. This is to be expected when coupling light into an optical fiber, although in this lab we have achieved efficiencies closer to 50% which we will aim to replicated for the eventual implementation. In Figure 16b, we have normalized the peaks before and after the fiber to a maximum of 1. Here we see that the pulse after the fiber has a rise time around 8 ns, a decrease by about 25%. This may be explained by the fact that the fiber coupling depends on both the power and mode of light, so the input beam must achieve both high enough power and a clean enough mode before the fiber accepts it.

## F. Measuring Power Efficiency

Now that we could generate fast pulses of light, the next step was to consider how to optimize the power efficiency into the diffracted beam. To characterize this, in Figure 17 we looked at power output as we varied the TTL pulse length (and thus the size of the RF packet) as well as the RF frequency.

In Figure 17a, we see that overall we get the most power out when operating at 140 MHz. The likely explanation is that this AOM has a center frequency of 140 MHz (despite being labeled as 200 MHz), so it produces the best efficiencies at this frequency, and power output drops off as the frequency deviates away. Additionally, we see that for all frequencies, there is a drop off in power

output for shorter pulses. This may be explained by the fact that for a shorter pulse, there are less nodes for the light to diffract off of, so it behaves more like multi-slit diffraction than Bragg diffraction. As pulse length increases, we effectively approach continuous wave mode so the power efficiency flattens out.

In Figure 17b, we have taken all of the data and normalized it with respect to the power output in continuous wave mode. Here we see that higher frequencies produce better normalized power efficiency. For higher frequencies, there are more nodes at the shorter pulse widths, so we might expect better efficiencies. This suggests that using a higher center frequency AOM, such as 400 MHz, may result in increased power output specifically at the short pulse range that we are interested in.

However, when taking this data, we did not take steps to ensure the RF power was the same for each RF frequency. If the RF power was significantly different in each trial, that could be another factor contributing to the trends we observe. There is reason to believe this could be the case since the AOM is listed as having a center frequency of 200 MHz, contradicting our observation that it performs best at 140 MHz. Future work should reproduce these measurements while controlling for RF power to verify these results.

### G. Calculating $\pi$ Pulse Duration

By now we have a good understanding of the pulse length and power that we can generate, so we want to see how short of  $\pi$  pulses we can produce. To do this, we model the pulses as in Figure 18a. For simplicity, we assume there is some rise time in which the power linearly increases to the maximum, then we can hold that power for some time before turning the pulse off, and then it linearly decreases to 0. Rabi frequency goes as the square root of power, as shown in Figure 18b, and to generate a  $\pi$  pulse we must tune the parameters such that the area under the curve is equal to  $\pi$ .

Thus, the two main parameters that will dictate how long of a  $\pi$  pulse we produce will be the maximum power level of the pulse and the rise time. However, as we have seen, power, pulse length, and rise time are all intrinsically dependent on each other, so it's difficult to project exactly what length  $\pi$  pulses we can achieve.

However, we can look at their effects in isolation. In Figure 19a we have set the rise time at 8 ns, which currently seems within reach for our system. We see that to get a 10 ns  $\pi$  pulse we would then need a max power of about 150 mW at the atoms.

With our current setup and power efficiencies, we make a conservative estimate that we can achieve a maximum power of around 75 mW at the atoms by sending 300 mW of power to the AOM, getting a maximum power of 50% in the first order beam, and then another 50% of that into the optical fiber. Holding the power constant at 75 mW, in Figure 19b we see that we would then need

a rise time of around 2.5 ns to get a 10 ns  $\pi$  pulse.

The conclusion is that we are currently close to this goal, but not quite able to achieve it. However, once we can improve our electronics and get more tunability over the rise time and width of our pulses, we will be able to run additional tests to hopefully find a configuration that allows for 10 ns pi-pulses. But, at the very least, we see that we can comfortably get 15 ns  $\pi$  pulses, which could still potentially allow for up to 100  $\hbar k$  separation in our interferometer.

Additionally, we can make a conservative approximation of the contrast we can achieve based on the probability of spontaneous emission given by  $P(t) = e^{-t/\tau}$  for some time  $t$  and lifetime  $\tau = 875$  ns. Assuming a 50% duty cycle, we approximate that for  $\pi$  pulses of duration  $T$ , the atoms are then in the excited state for time  $T$  before the next  $\pi$  pulse addresses them. Then the probability of spontaneous emission for  $N$  many  $\pi$  pulses is given by  $(e^{-t/\tau})^N$ . Then with 15 ns pulses, for 100 $\hbar k$  separation (50  $\pi$  pulses) we could achieve contrast up to 0.42. If we can achieve 10 ns pulses, for the same 100 $\hbar k$  separation we could improve our contrast up to 0.56. While these are likely underestimates, these contrast projections are still promising.

## IV. FUTURE OUTLOOK

To recap, we have so far demonstrated that we can generate 10 ns pulses, and we have established rise time and power efficiency requirements to get  $\pi$  pulses of 10 ns. While that is not quite possible at the moment, future work will include developing electronics to produce faster rise time, shorter pulses with more tunability to allow for further testing and to potentially find a setting that can achieve this goal.

As we have noted, the current limitation is set by the switch, but there do not seem to be faster switches available for purchase. The solution we are currently working on is to forego the switch entirely and to generate the RF pulse directly. To do this, we will effectively build an arbitrary waveform generator using a field-programmable gate array (FPGA). Additionally, as previously noted, controlling the phase of the pulses is important. While the switch did not allow for control over the phase, by writing the wave packet from scratch, the FPGA will allow us to reproducibly control and tune the phase of each pulse.

At that point, we will be ready to implement this into the actual machine to test with the atoms and confirm how fast of  $\pi$  pulses we can achieve, as well as their efficiencies. Then we will be ready to reproduce all of this with a second AOM to provide a second pulse source, which we can then use to perform LMT clock AI with ytterbium atoms.

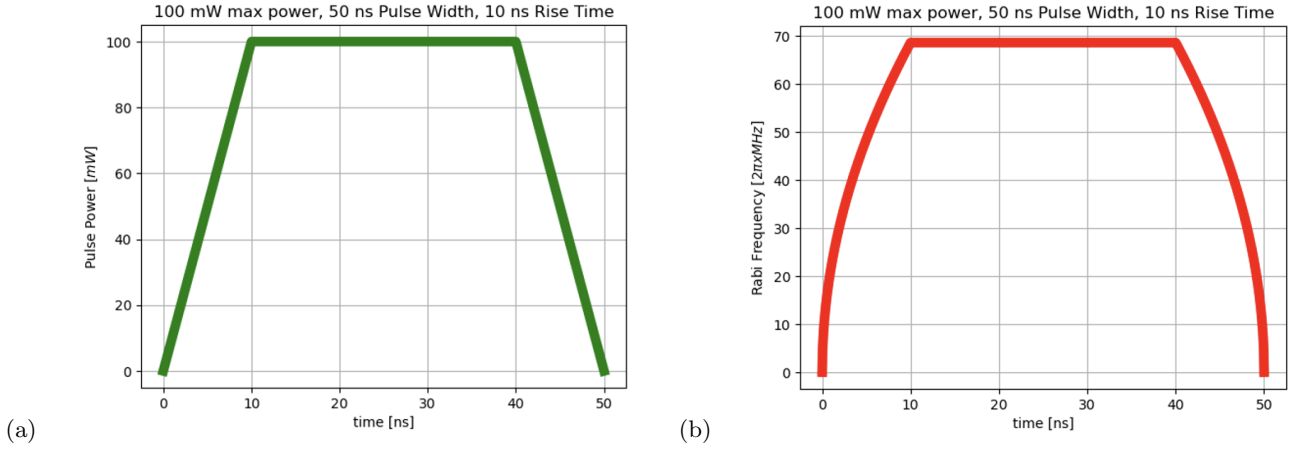


FIG. 18: Approximate beam pulse profile (a) and corresponding Rabi frequency (b) over time for a 50 ns pulse, 10 ns rise time, and 100 mW maximum power.

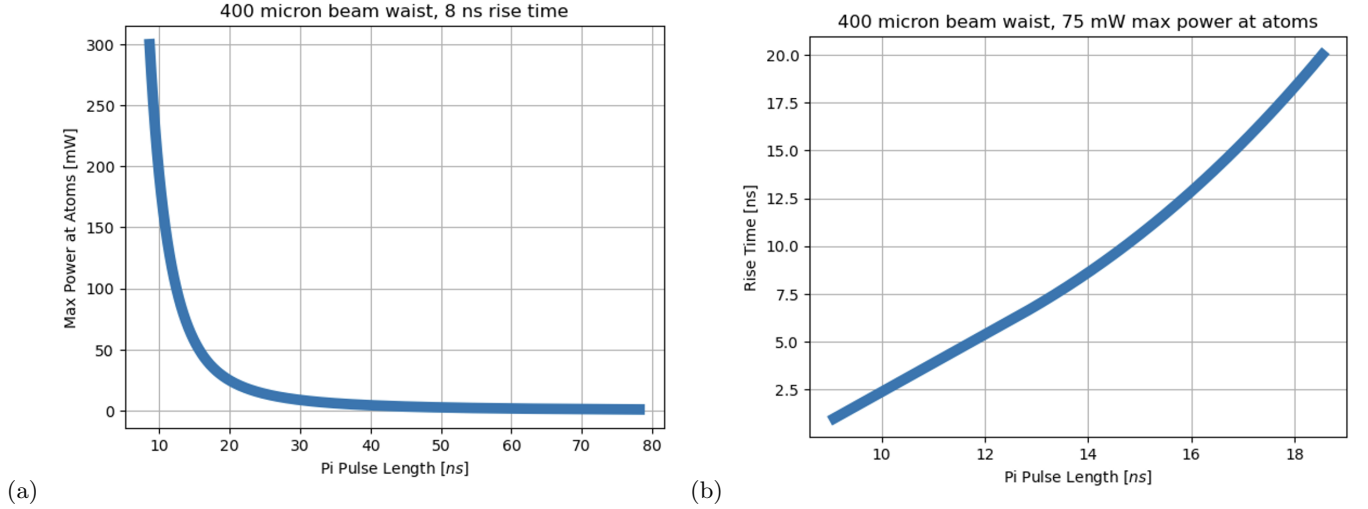


FIG. 19: Pi pulse length calculations for various (a) maximum power and (b) rise time values.

## V. ACKNOWLEDGEMENTS

Thank you to the NSF for funding this research, as well as the University of Washington Physics Department, and REU coordinators Dr. Gray Rybka and Dr. Arthur Barnard for helping organize and run this program. Thank you to the Institute for Nuclear Theory

administration, especially Kimberlee Choe and Morgan Miller, for assisting with the administrative parts of the program. And thank you to Dr. Subhadeep Gupta and the atom interferometry group, especially Emmett Hough, Tahiyat Rahman, and Richard Kim for the support throughout this project.

- 
- [1] A. D. Cronin, J. Schmiedmayer, and D. E. Pritchard, Optics and interferometry with atoms and molecules, *Reviews of Modern Physics* **81**, 1051 (2009), publisher: American Physical Society.
  - [2] L. Qiu, H. Yuan, and S. Wu, High-fidelity Raman matterwave control by composite biased rotations, *Physical Review Research* **5**, 043094 (2023), publisher: American Physical Society.
  - [3] F. Fitzek, J.-N. Kirsten-Siemß, E. M. Rasel, N. Gaaloul, and K. Hammerer, Accurate and efficient Bloch-oscillation-enhanced atom interferometry, *Physical Review Research* **6**, L032028 (2024), publisher: American Physical Society.
  - [4] C. J. Foot, *Atomic Physics* (Oxford University Press, 2005).
  - [5] B. Plotkin-Swing, D. Gochnauer, K. E. McAlpine, E. S. Cooper, A. O. Jamison, and S. Gupta, Three-path atom

- interferometry with large momentum separation, *Phys. Rev. Lett.* **121**, 133201 (2018).
- [6] A. H. Hansen, A. Khramov, W. H. Dowd, A. O. Jamison, V. V. Ivanov, and S. Gupta, Quantum degenerate mixture of ytterbium and lithium atoms, *Phys. Rev. A* **84**, 011606 (2011).
- [7] A. O. Jamison, B. Plotkin-Swing, and S. Gupta, Advances in precision contrast interferometry with yb bose-einstein condensates, *Phys. Rev. A* **90**, 063606 (2014).
- [8] D. Gochnauer, T. Rahman, A. Wirth-Singh, and S. Gupta, Interferometry in an atomic fountain with ytterbium bose-einstein condensates, *Atoms* **9**, 10.3390/atoms9030058 (2021).
- [9] S. Gupta, A. E. Leanhardt, A. D. Cronin, and D. E. Pritchard, Coherent manipulation of atoms with standing light waves, *Comptes Rendus de l'Académie des Sciences - Series IV - Physics* **2**, 479 (2001).
- [10] T. Rahman, A. Wirth-Singh, A. Ivanov, D. Gochnauer, E. Hough, and S. Gupta, Bloch oscillation phases investigated by multipath stückelberg atom interferometry, *Physical Review Research* **6**, 10.1103/physrevresearch.6.1022012 (2024).
- [11] K. E. McAlpine, D. Gochnauer, and S. Gupta, Excited-band bloch oscillations for precision atom interferometry, *Phys. Rev. A* **101**, 023614 (2020).
- [12] D. Gochnauer, K. E. McAlpine, B. Plotkin-Swing, A. O. Jamison, and S. Gupta, Bloch-band picture for light-pulse atom diffraction and interferometry, *Phys. Rev. A* **100**, 043611 (2019).
- [13] J. D. Rudolph, T. Wilkason, M. Nantel, H. F. Swan, C. M. Holland, Y. Jiang, B. E. Garber, S. P. Carman, and J. M. Hogan, Large momentum transfer clock atom interferometry on the 689 nm intercombination line of strontium, *Phys. Rev. Lett.* **124**, 10.1103/physrevlett.124.083604 (2020).
- [14] R. Paschotta, Acousto-optic modulators, *RP Photonics Encyclopedia*.